Check for updates

ADVANCED MATERIALS
www.advmat.de

Spin-polarized Acidic Water Electrolysis with Antenna-Reactor Plasmonic Electrocatalysts

Kyunghee Chae, Heejun Lee, Wen-Tse Huang, Jaehyun Son, Bertrand Pavageau, Tae-Hyun Kim, Seung-eun Lee, Jeongwon Kim, Jooho Moon,* Ru-Shi Liu,* Joonho Bang,* and Dong Ha Kim**

Water electrolysis, driven by renewable electricity, offers a sustainable path for hydrogen production. However, efficient bifunctional electrocatalysts are needed to overcome the high overpotentials of both the oxygen evolution reaction and hydrogen evolution reaction. To address this, a novel catalyst system is developed integrating plasmonic nanoreactors with chirality-induced spin selectivity. In this system, chiral Au nanoparticles act as antennae, while single-atom iridium serves as the catalytic reactor, achieving a 3.5 fold increase in reaction kinetics (at 1.57 V vs RHE) compared to commercial IrO_2 catalysts and enhancing durability by over 4.8 times relative to conventional Pt/C || IrO_2 systems. Density functional theory and *operando* X-ray absorption spectroscopy reveal that plasmon-driven spin alignment polarizes the Ir atom, significantly enhancing stability (>480 h at 100 mA cm^{-2}) under acidic conditions. This work represents a major advance in spin polarization for plasmonic electrocatalysis, offering a new route to sustainable energy solutions.

1. Introduction

Electrochemical water splitting, powered by renewable electricity, offers a promising path toward a sustainable, fossil-fuel-free global energy system.[1–4] However, its scalability is constrained by the substantial energy demands associated with the sluggish kinetics of the oxygen evolution reaction (OER) and the hydrogen evolution reaction (HER).[5,6] To address these challenges, the development of efficient bifunctional electrocatalysts capable of facilitating both OER and HER with low overpotentials in a unified electrolyte is essential. Such catalysts not only improve overall efficiency but also reduce costs and streamline the fabrication process of water-splitting devices.[7] Among the two half-reactions, OER remains the more challenging step due to its complex multi-electron transfer mechanism.[8]

Among catalysts for the OER, iridium is regarded as the most effective due to its exceptional catalytic activity and stability, making iridium single-atom catalysts (Ir SACs) a particularly promising advancement.[9] These catalysts have garnered significant attention for their ability to reduce iridium consumption while improving OER performance through electronic modulation and optimized ligand adsorption.[10,11] Despite these benefits, traditional approaches often overlook the pivotal role of electron spin in reaction

K. Chae, J. Kim, D. H. Kim
Department of Chemistry and Nanoscience
Division of Molecular and Life Sciences
College of Natural Sciences
Ewha Womans University
52, Ewhayeodae-gil, Seoul, Seodaemun-gu 03760, Republic of Korea
E-mail: kimgarden@ewha.ac.kr; dhkim@ewha.ac.kr

H. Lee, J. Bang
Department of Materials Engineering and Convergence Technology
Gyeongsang National University
Jinju 52828, Republic of Korea
E-mail: bang@gnu.ac.kr

The ORCID identification number(s) for the author(s) of this article can be found under https://doi.org/10.1002/adma.202507658

© 2025 The Author(s). Advanced Materials published by Wiley-VCH GmbH. This is an open access article under the terms of the Creative Commons Attribution-NonCommercial-NoDerivs License, which permits use and distribution in any medium, provided the original work is properly cited, the use is non-commercial and no modifications or adaptations are made.

DOI: 10.1002/adma.202507658

W.-T. Huang, R.-S. Liu
Department of Chemistry
National Taiwan University
Taipei 106, Taiwan
E-mail: rsliu@ntu.edu.tw

J. Son, J. Moon
Department of Materials Science and Engineering
Yonsei University
50 Yonsei-ro Seodaemun-gu, Seoul 03722, Republic of Korea
E-mail: jmoon@yonsei.ac.kr

B. Pavageau
Rhodia Lab of Future
part of the Syensqo Group
178 Avenue du Dr Albert Schweitzer, Pessac 33600, France

T.-H. Kim, S.-eun Lee
Ewha-Syensqo R&I Center
150 Bukahyun-ro, Seoul, Seodaemun-gu 03759, South Korea

J. Kim
Department of Chemistry
Northwestern University
Evanston, IL 60208, USA

kinetics, particularly considering the triplet ground state of oxygen.[12,13] To further enhance OER performance, it is crucial to optimize the spin-dependent environment around Ir SACs and their interaction with catalytic supports.

A breakthrough in this area is the use of chiral molecules to generate spin-polarized currents via the chirality-induced spin selectivity (CISS) effect.[14,15] The CISS effect aligns the spins of electrons or holes passing through chiral molecules, lowering OER overpotentials and suppressing hydrogen peroxide formation—all without the need for external magnetic fields.[16–18] Beyond molecular chirality, this concept has been extended into nanoplasmonics, which exhibit localized surface plasmon resonance (LSPR).[19–21] LSPR enables the utilization of near-field or thermal energy to facilitate chemical reactions, presenting an opportunity to further enhance catalytic efficiency. While CISS-based OER has demonstrated success, the deliberate design of chiral plasmonic catalysts for water splitting remains relatively unexplored, highlighting the need for a deeper understanding of the underlying mechanisms.

In this study, we present a bifunctional chiral plasmonic electrocatalyst featuring iridium single atoms (Ir SA) as a reactor, synthesized via a straightforward electrodeposition process (Figure S1, Supporting Information), combined with chiral Au nanoflowers (L-Au NF) serving as an antenna, deposited onto a titanium (Ti) felt substrate, using L-cysteine as a chiral inducer. The electrodeposition process is carefully controlled to ensure the optimal loading of Ir single atoms, resulting in an optimized catalyst structure. When applied to overall water splitting, the Ir SA/L-Au NF/Ti || Ir SA/L-Au NF/Ti electrode exhibits remarkable stability, maintaining high performance for over 480 h at a current density of 100 mA cm^{-2}, surpassing the performance of conventional Pt/C || IrO_2 systems.

The catalyst's exceptional performance can be attributed to three key factors: 1) facile transfer of hot carriers from the Au NPs to the reactor catalyst under light, facilitated by the plasmonic effect (**Figure 1**a); 2) well-aligned spins of Ir atoms on the surface, enabling effective spin transfer to adsorbed molecules, particularly oxygen, via the CISS effect, as demonstrated by density functional theory (DFT) calculations (Figure 1b,c); and 3) the high intrinsic catalytic activity of Ir single atoms. *Operando* X-ray absorption spectroscopy (XAS) further corroborates these findings, revealing dynamic electronic structure changes during operation, which play a crucial role in enhancing the catalyst's performance.

2. Results and Discussion

2.1. Fabrication and Characterization

Scanning electron microscopy (SEM) (Figures S2 and S3, Supporting Information) and transmission electron microscopy (TEM) (Figure S4, Supporting Information) analyses revealed a uniform coverage of Au NFs with a lattice spacing corresponding to the (111) plane, affirming the nanocrystalline nature of the Au. X-ray diffraction (XRD) spectra (Figure S5, Supporting Information) of the samples confirmed their highly crystalline structures without any discernible Ir peak, attributed to the low Ir loading, quantified as ≈1.4 wt.% by inductively coupled plasma-mass spectroscopy (ICP-MS) for both achiral Ir SA/DL-Au NF and chiral Ir SA/L-Au NF catalysts (Table S1, Supporting Information). The TEM results, in agreement with the XRD findings, indicated that the integration of Ir single atoms did not alter the phase structure of the chiral Au NFs. Further structural analysis at the atomic scale was conducted using high-angle annular dark field scanning transmission electron microscopy (HAADF-STEM) (**Figure 2**a), revealing no noticeable Ir metal particles. Elemental mapping (Figure 2b; Figure S6, Supporting Information) showed a homogeneous distribution of Au and Ir, with the dispersion of Ir single atoms on the surface of the Au NFs, indicating successful fabrication of the bifunctional electrocatalyst.

X-ray photoelectron spectroscopy (XPS) was utilized to elucidate the chemical state of our synthesized catalysts, as illustrated in Figure 2c and Figure S7 (Supporting Information). The XPS analysis revealed that the Ir 4f spectrum of the Ir SA/L-Au NF catalyst was split into two doublets – Ir $4f_{7/2}$ and Ir $4f_{5/2}$.[22] Notably, these peaks, located at 61.1 eV for Ir $4f_{7/2}$ and 63.8 eV for Ir $4f_{5/2}$, exhibited a shift to lower binding energies compared to IrO_2, which presents peaks at 61.7 eV for Ir $4f_{7/2}$ and 64.6 eV for Ir $4f_{5/2}$.[3,23] This shift is indicative of electron transfer from iridium to gold, aligning well with the characteristics of a bimetallic Ir-Au system.[23,24]

The local atomic and electronic structures of a single Ir atom on a chiral L-Au nanoflower (Ir-SA/L-Au NF) were thoroughly investigated using X-ray absorption fine structure spectroscopy (XAFS). Figure 2d compares the X-ray absorption near-edge fine structure (XANES) spectrum of Ir at the Ir L_3-edge among Ir-SA/L-Au NF, IrO_2, and Ir foil. The XANES spectrum of Ir-SA/L-Au NF shows a resemblance to that of Ir bulk metal, suggesting that most Ir atoms are predominantly in a metallic state.[25] Notably, the white line in the XANES spectrum of Ir-SA/L-Au NF shifts by 0.5 eV toward higher energy compared to Ir foil (0), while it shifts by 0.9 eV toward lower energy relative to IrO_2 (+4). This white line intensity is generally associated with the density of d orbital states, and its order—Ir-SA/L-Au NF > IrO_2 > Ir foil—indicates the presence of unsaturated Ir sites or IrO_x species (Figure S8, Supporting Information).[26] The increased

J. Bang
School of Materials Science and Engineering
Gyeongsang National University
Jinju 52828, Republic of Korea
D. H. Kim
College of Medicine
Ewha Womans University
25, Magokdong-ro 2-gil, Gangseo-gu, Seoul 07804, Republic of Korea
D. H. Kim
Gradutate Program in Innovative Biomaterials Convergence
Ewha Womans University
52 Ewhayeodae-gil, Seoul, Seodaemun-gu 03760, Republic of Korea
D. H. Kim
Basic Sciences Research Institute (Priority Research Institute)
Ewha Womans University
Seoul 03760, Republic of Korea
D. H. Kim
Nanobio • Energy Materials Center (National Research Facilities and Equipment Center)
Ewha Womans University
Seoul 03760, Republic of Korea

© 2025 The Author(s). Advanced Materials published by Wiley-VCH GmbH

15214095, 2025, 39, Downloaded from https://advanced.onlinelibrary.wiley.com/doi/10.1002/adma.202507658 by Ewha Womans University Library, Wiley Online Library on [13/01/2026]. See the Terms and Conditions (https://onlinelibrary.wiley.com/terms-and-conditions) on Wiley Online Library for rules of use; OA articles are governed by the applicable Creative Commons License

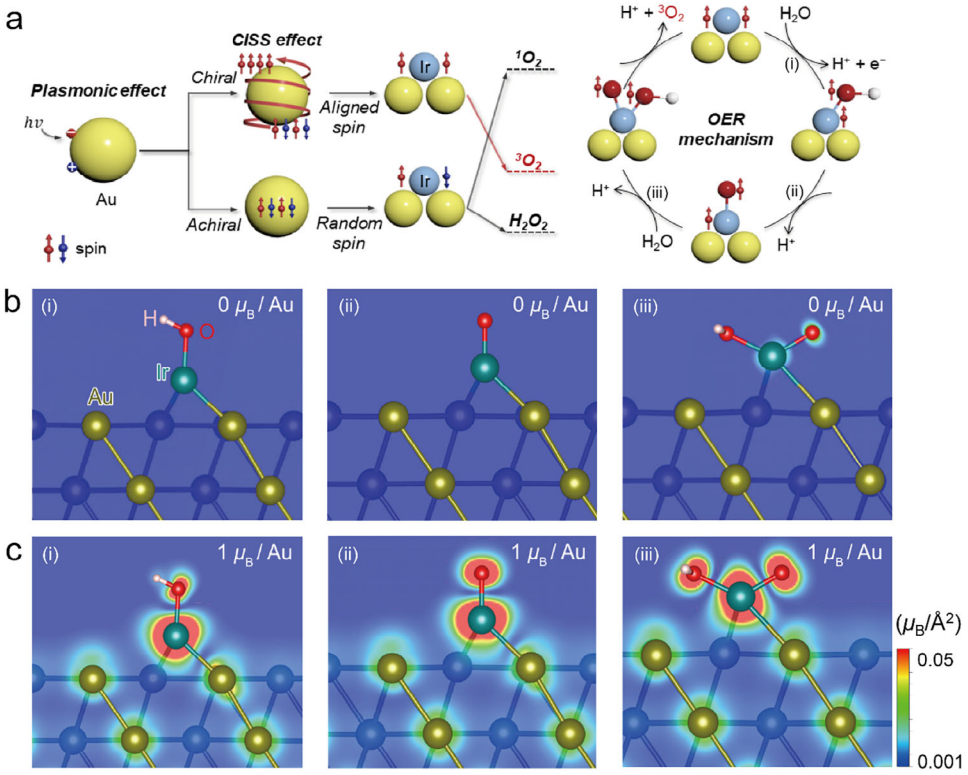


Figure 1. Overview of the CISS effect in the OER mechanism. a) Schematic illustration of the CISS effect in chiral plasmonic materials (left) and the overall mechanism of the OER process with aligned spin (right). b) Magnetic density maps of OER intermediates on a non-spin-polarized Au surface. c) Magnetic density maps of OER intermediates on a spin-polarized Au surface.

number of empty d orbital states (d holes) in Ir-SA/L-Au NF suggests improved electrocatalytic performance.[25,27]

Further insights are provided by the wavelet transform of the extended X-ray absorption fine structure (EXAFS) data, which offers a detailed view in both real-space (R space) and reciprocal-space (k space). The wavelet transform intensity peaks occur ≈11 and 6 Å^{-1}, corresponding to Ir—Ir and Ir—O contributions, respectively. In the IrO_2 sample, the R-space EXAFS data (Figure 2e) show a clear Ir—O peak at ≈1.5–2.0 Å. In contrast, the wavelet transform for Ir-SA/L-Au NF (Figure 2f) shows a prominent peak near 7.5 Å^{-1}, representing Ir—Au interactions, consistent with the R-space peak at ≈2.5–3.0 Å. Notably, no corresponding Ir—O signal is observed in the Ir-SA/L-Au NF sample at the position expected from IrO_2 (≈1.5–2.0 Å in R-space), indicating that Ir—O coordination is not dominant in this sample. A weak feature at ≈1.07 Å in the R space of Ir-SA/L-Au NF is attributed to a background artifact, likely resulting from the low signal intensity of the Ir-SA/L-Au NF sample, which made it challenging to fully remove background contributions during data processing.

2.2. CISS Effect of Ir SA/Chiral Au NF

To assess the CISS effect in our Ir SA/chiral Au NF electrodes, we fabricated chiral Au NF electrodes using the same electrodeposition method on ITO substrates. The circular dichroism (CD) spectra in **Figures** 3a and S11 and S12 (Supporting Information) in detail, display mirror symmetry, reflecting the opposing chirality of the Au NFs grown with D-cysteine:Au^{3+} (D-Au NF) and L-cysteine:Au^{3+} (L-Au NF).[28] Notably, these spectra were obtained from separately prepared films, where slight variations in thickness or morphology may affect the mirror symmetry. In contrast, DL-cysteine:Au^{3+} complexes produced an achiral film.

We probed the spin-dependent current of chiral Au NFs using magnetic conductive probe atomic force microscopy (mc-AFM), as shown in Figure 3b. Ferromagnetic CoCr tips, pre-magnetized northward and southward, enabled the measurement of spin-polarized currents over a voltage range from −1.0 to 1.0 V. For reliability, over 30 different points on each sample were assessed. With the Ir SA/L-Au NF, currents under the Tip_{Up} condition notably exceeded those in the Tip_{Down} setting, indicating a preferential selection for up-spin charge carriers (Figure 3d). In contrast, the Ir SA/D-Au NF displayed higher currents with downward tip magnetization (Figure S13b, Supporting Information). No significant changes in current were observed for the achiral Ir SA/DL-Au NF under varying tip magnetizations (Figure 3c). The spin polarization (SP) of the Ir SA/Au NF was subsequently quantified using a specific Equation (1).

$$SP\,(\%) = (IUp - IDown) / (IUp + IDown) \times 100\% \quad (1)$$

where I_{Up} and I_{Down} are currents measured when the CoCr tip was magnetized along the north and south orientations, respectively.[29] Figure 3e and Figure S13 (Supporting Information) demonstrate the distinct spin-dependent current

© 2025 The Author(s). Advanced Materials published by Wiley-VCH GmbH

15214095, 2025, 39, Downloaded from https://advanced.onlinelibrary.wiley.com/doi/10.1002/adma.202507658 by Ewha Womans University Library, Wiley Online Library on [13/01/2026]. See the Terms and Conditions (https://onlinelibrary.wiley.com/terms-and-conditions) on Wiley Online Library for rules of use; OA articles are governed by the applicable Creative Commons License

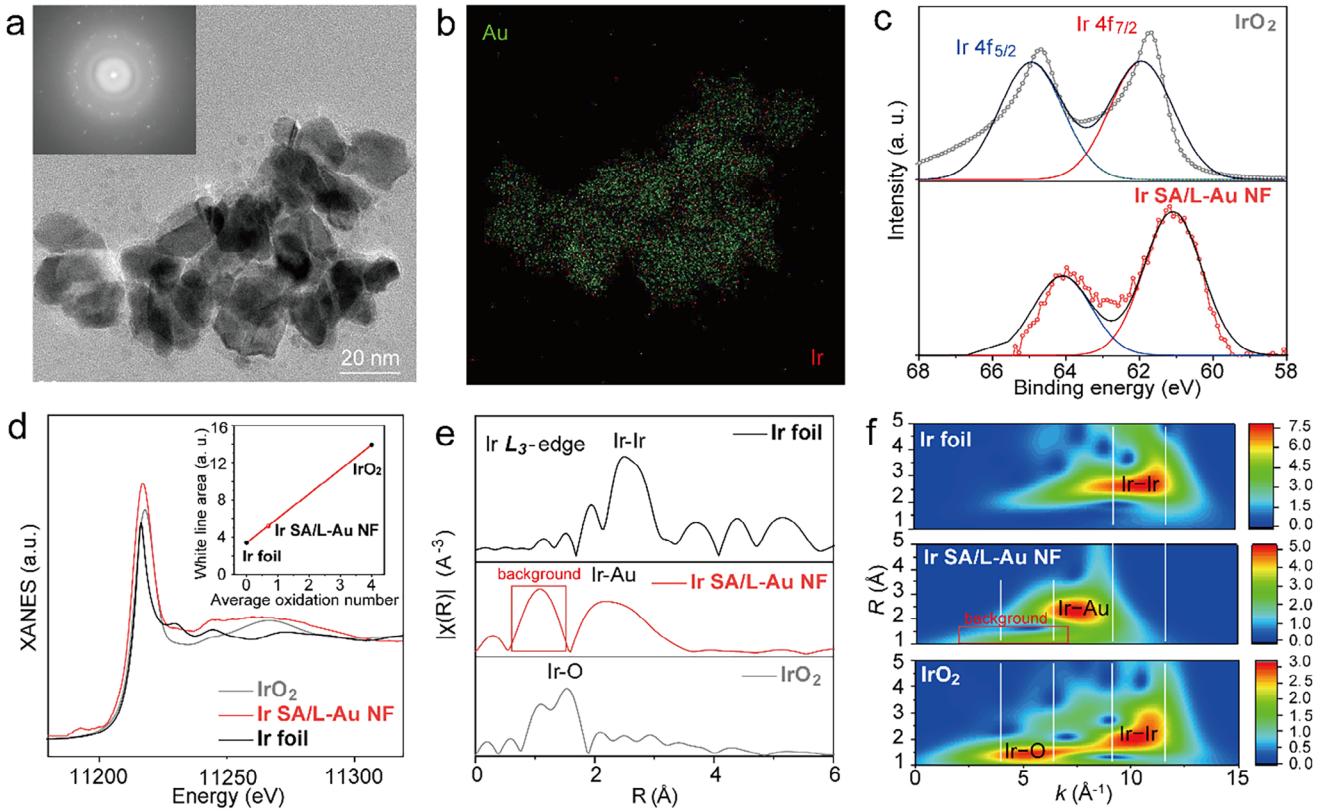


Figure 2. Characterizations of Ir SA/chiral Au NF/Ti felt electrode. a) HAADF-STEM image of Ir SA/L-Au NF and corresponding fast Fourier transformation (FFT) pattern. b) STEM-EDS elemental mapping image of Ir SA/L-Au NF. c) Ir 4f XPS spectra of Ir SA/L-Au NF and IrO_2 reference sample. d) Ir L_3-edge XANES spectra of Ir-SA/L-Au NF in reference to Ir foil and IrO_2. e) Wavelet transform for the k^2-weighted Ir L_3-edge EXAFS signal. f) Fourier transform of k^2-weighted EXAFS spectra of Ir L_3-edge.

behavior of the Ir SA/L-Au NF, exhibiting an average spin polarization (SP) of 90.8%. In contrast, the Ir SA/DL-Au NF showed no variation between I_{Up} and I_{Down} currents, indicating that the spin-dependent current behavior is attributed to the induced chirality of the Au NF, a direct consequence of the CISS effect.[30]

2.3. Electrochemical Performance of Ir SA/Chiral Au NF/Ti Electrode

The electrocatalytic OER activities of Ir SA/chiral Au NF electrodes were evaluated in 0.5 M H_2SO_4 using a three-electrode system at a scan rate of 5 mVs^{-1}. Linear sweep voltammetry (LSV) curves highlighted the OER activities of Ir SA/L-Au NF and reference samples with and without light irradiation (**Figure** 4a). Notably, the DL-Au NF without Ir SA doping exhibited minimal OER activity, while the current density progressively increased with the incorporation of Ir SA (Ir SA/DL-Au NF), the application of chirality (Ir SA/L-Au NF), and further enhancement under light irradiation (Ir SA/L-Au NF light) (Figures S14–S17, Supporting Information). Moreover, the Ir SA/L-Au NF under light conditions demonstrated significantly better acidic OER activity compared to commercial IrO_2 (Figure S18, Supporting Information). For example, Ir SA/L-Au NF under light exhibited a maximum mass activity of 53.3 mA mg_{Ir}^{-1} at 1.575 V, 3.5 times higher than IrO_2. The combination of Ir active sites and chiral plasmonic effects facilitated highly efficient water oxidation in acidic media.[28]

To better understand the OER kinetics, we analyzed Tafel plots of Ir SA/L-Au NF under light, which exhibited a slope of 77.9 mA dec^{-1}, lower than that of Ir SA/L-Au NF in dark conditions (79.1 mA dec^{-1}), Ir SA/DL-Au NF (81.1 mA dec^{-1}), and DL-Au NF without Ir SA doping (170.7 mA dec^{-1}) (Figure 4b; Figure S18d, Supporting Information). These results suggest a more efficient OER pathway stimulated by the synergistic effects of Ir single atoms, chirality, and plasmonic enhancement. We also evaluated the electrochemical double-layer capacitance (C_{dl}) to determine the electrochemically active surface area (ECSA) (Figure 4c; Figures S19 and S20, Supporting Information). Ir SA/L-Au NF showed a C_{dl} of 10.8 mF cm^{-2}, which was higher than those of Ir SA/DL-Au NF (6.274 mF cm^{-2}) and DL-Au NF (1.77 mF cm^{-2}), indicating a higher ECSA and a more effective catalyst.[31] Electrochemical impedance spectroscopy (EIS) measurements also indicated faster OER kinetics on Ir SA/L-Au NF under light, suggesting enhanced electrical conductivity due to the synergistic effects of Ir single atoms and chiral plasmonics (Figure S21, Supporting Information).

Two key performance metrics for electrocatalysts are specific activity and turnover frequency (TOF).[27] At 1.575 V versus RHE,

© 2025 The Author(s). Advanced Materials published by Wiley-VCH GmbH

15214095, 2025, 39, Downloaded from https://advanced.onlinelibrary.wiley.com/doi/10.1002/adma.202507658 by Ewha Womans University Library, Wiley Online Library on [13/01/2026]. See the Terms and Conditions (https://onlinelibrary.wiley.com/terms-and-conditions) on Wiley Online Library for rules of use; OA articles are governed by the applicable Creative Commons License

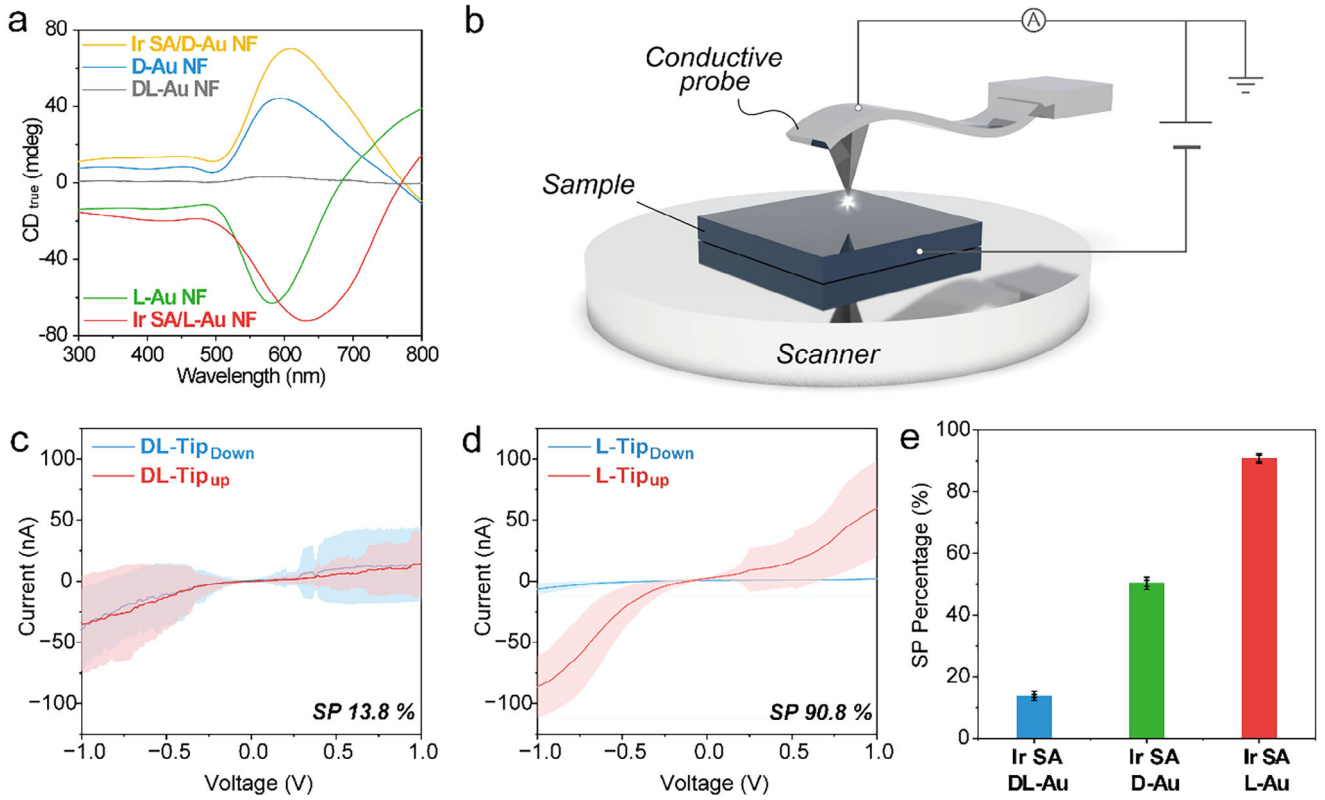


Figure 3. Chiroptical properties of Ir SA/chiral Au NF/Ti felt electrode. a) CD_{true} spectra of L/D/DL-cysteine Au NF and Ir SA/chiral Au NF on an ITO substrate. b) Schematic illustration of the mc-AFM measurement. *I–V* curves of c) Ir SA/DL-cysteine Au NF and d) Ir SA/L-cysteine Au NF films with spin polarization percentage (SP%) in the range of −1.0–+1.0 V. The CoCr tip was magnetized along the upward (spin-up, red) or downward (spin-down, blue) orientation. The average *I–V* curve recorded over 30 scans at different points is shown. e) Spin polarization percentage (SP%) as a function of applied bias of (c) Ir SA/DL-cysteine Au NF and (d) Ir SA/L-cysteine Au NF films, calculated by excluding the low-bias region (−0.3–+0.3 V) to avoid contribution from asymptotic current regions and low signal-to-noise effects.

Ir SA/L-Au NF under light exhibited the highest specific activity (60.2 mA cm^{-2}), ≈2.8 and 6.8 times higher than those of Ir SA/L-Au NF in the dark (21.6 mA cm^{-2}) and Ir SA/DL-Au NF (8.85 mA cm^{-2}), respectively (Figure 4d). Additionally, Ir SA/L-Au NF under light demonstrated a high intrinsic activity, as indicated by a TOF value normalized to Ir sites per geometric area of 0.03 s^{-1}. To ensure a fair comparison of intrinsic OER activity, we also normalized current density to ECSA. The corresponding ECSA-normalized LSV curves and overpotentials at 10 mA cm^{-2} are presented in Figure S22 (Supporting Information). These results reaffirm the superior intrinsic OER activity of Ir SA/L-Au NF under light, even after accounting for surface area difference.

When targeting a current density of 10 mA cm^{-2}, Ir SA/L-Au NF under light required an overpotential of 272.6 mV, lower than the overpotentials of Ir SA/L-Au NF in the dark (313.8 mV) and Ir SA/DL-Au NF (340 mV) (Figure S23, Supporting Information). Notably, the low overpotential of Ir SA/L-Au NF under light was even lower than that of commercial IrO_2 (311.3 mV) (Figure S18e, Supporting Information). Additionally, Ir SA/L-Au NF under light exhibited the lowest onset potential, highlighting the fastest OER activation rate among the catalysts tested. Stability testing revealed remarkable durability, as Ir SA/L-Au NF under light exhibited only an insignificant increase in overpotential after a 10 h chronoamperometric test at 10 mA cm^{-2} (Figure S24, Supporting Information), underscoring its robustness as an OER electrocatalyst.

Furthermore, Ir SA/L-Au NF showed enhanced selectivity for OER processes by suppressing H_2O_2 production, as shown in Figure 4e and Figure S25 (Supporting Information). The UV–vis absorption spectra in Figure 4e were obtained by titrating the electrolyte solution with $TiOSO_4$ after electrochemical testing. $TiOSO_4$ selectively reacts with H_2O_2 to form a yellow-colored peroxotitanium complex that absorbs at ≈405 nm, allowing quantification of H_2O_2 formation.[32] The much lower absorbance observed for Ir SA/L-Au NF (light) at this wavelength indicates suppressed H_2O_2 production, highlighting improved OER selectivity. This effect reinforces the relationship between the CISS effect and the superior OER activity of the Ir SA/L-Au NF catalyst.[32]

To further benchmark the OER activity of Ir SA/L-Au NF, we synthesized an Ir SA/Ti electrode (only Ir SA supported on Ti felt) and evaluated its electrocatalytic performance under the same acidic conditions, As shown in Figure S26 (Supporting Information), Ir SA/ Ti exhibited significantly higher overpotential (375.5 mV at 10 mA cm^{-2}) and lower current density (28.7 mA cm^{-2} at 1.575 V) than Ir SA/L-Au NF. Its tafel slope (104.8 mV dec^{-1}) was also higher, indicating less favorable reaction kinetics. These results clearly demonstrate the innovative role of

© 2025 The Author(s). Advanced Materials published by Wiley-VCH GmbH

15214095, 2025, 39, Downloaded from https://advanced.onlinelibrary.wiley.com/doi/10.1002/adma.202507658 by Ewha Womans University Library, Wiley Online Library on [13/01/2026]. See the Terms and Conditions (https://onlinelibrary.wiley.com/terms-and-conditions) on Wiley Online Library for rules of use; OA articles are governed by the applicable Creative Commons License

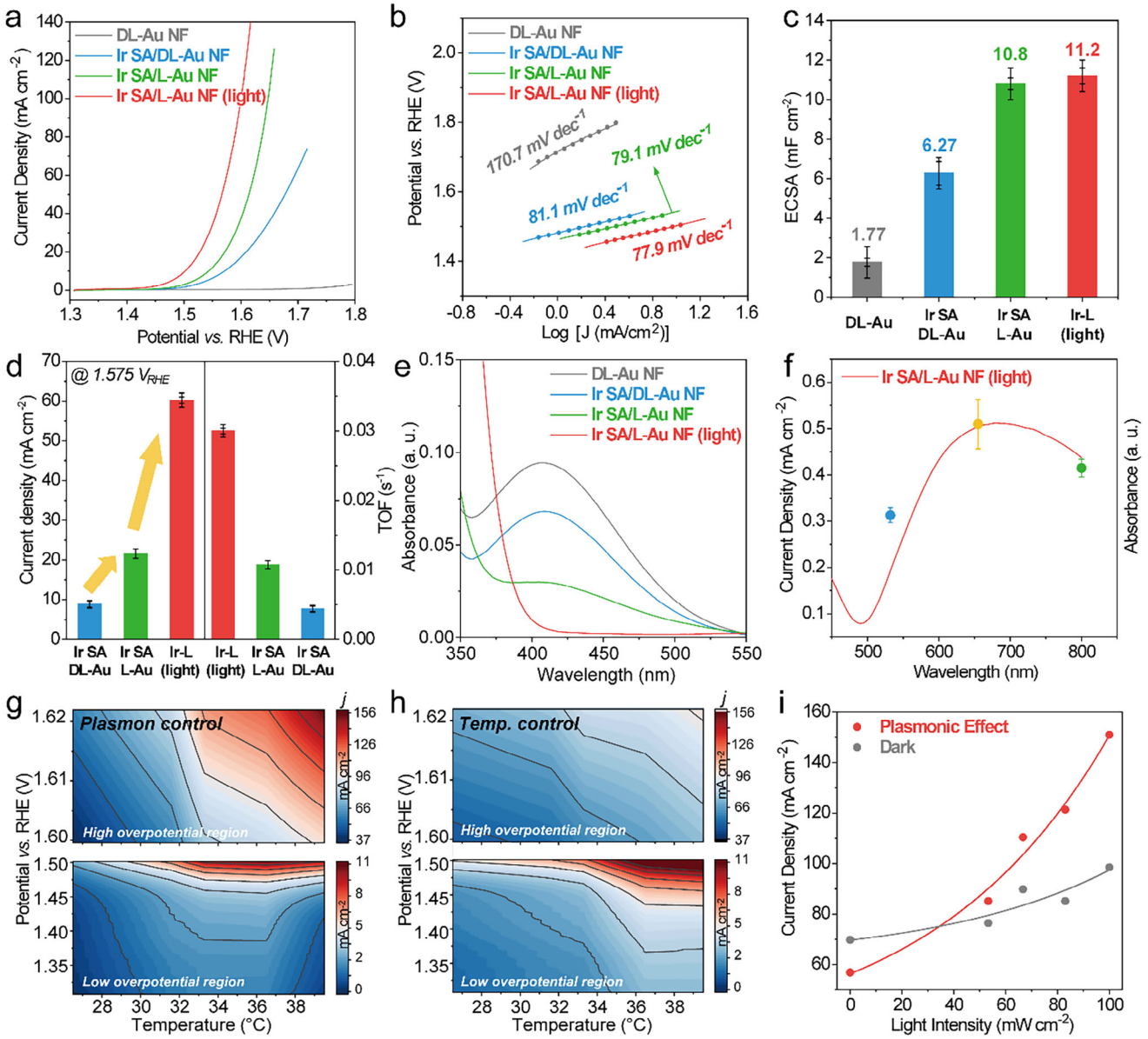


Figure 4. Electrochemical OER of Ir SA/chiral Au NF/Ti felt electrode. a) LSV curves recorded to determine geometric OER activity of DL-Au NF, Ir SA/DL-Au NF, and Ir SA/L-Au NF with and without illumination. b) Tafel plots corresponding to (a). c) Comparison of the ECSA of achiral and chiral Ir SA/Au NF/Ti felt with and without illumination. d) Specific activities; TOF values at 1.575 V versus RHE. e) UV–vis absorption spectra after the titration with $TiOSO_4$-containing aqueous solution of the electrolytes after the electrochemical measurement using DL-Au NF, Ir SA/DL-Au NF, and Ir SA/L-Au NF with and without illumination. f) Current density of Ir SA/L-Au NF/Ti felt with different wavelengths of 532, 655, and 808 nm. g) LSV curves recorded to determine OER activity with different light intensities from dark to 100 mW cm^{-2}. h) LSV curves recorded to determine OER activity with different temperatures corresponding to (g). i) OER activity from the plasmonic effect corresponding to (g) and (h).

chiral plasmonic Au nanoframes in enhancing OER performance beyond what can be achieved with Ir SA alone. The dramatic improvement in both activity and kinetics for Ir SA/L-Au NF (light) underscores the critical contribution of the CISS effect and LSPR-enhanced charge dynamics in accelerating the OER pathway.

To elucidate the role of photogenerated hot electrons from the Au NFs in enhancing OER performance, we conducted excitation-wavelength-dependent OER activity measurements (Figure 4g–i; Figures S27 and S28, Supporting Information). The current densities observed at 1.575 V across various wavelengths closely mirrored the absorbance profile of Ir SA/L-Au NF. This finding indicates that the light-enhanced OER activity is driven primarily by the LSPR effect inherent to Au NFs. To differentiate between plasmon-induced hot electrons and photothermal effects in catalysis, we compared photocatalytic and thermocatalytic activities while maintaining identical surface temperatures through both light illumination and external heating.[33,34] For OER, the current densities in thermocatalytic reactions were lower than those in photocatalytic reactions at the same temperature (Figure 4g–i), suggesting that plasmon-induced hot carriers

© 2025 The Author(s). Advanced Materials published by Wiley-VCH GmbH

15214095, 2025, 39, Downloaded from https://advanced.onlinelibrary.wiley.com/doi/10.1002/adma.202507658 by Ewha Womans University Library, Wiley Online Library on [13/01/2026]. See the Terms and Conditions (https://onlinelibrary.wiley.com/terms-and-conditions) on Wiley Online Library for rules of use; OA articles are governed by the applicable Creative Commons License

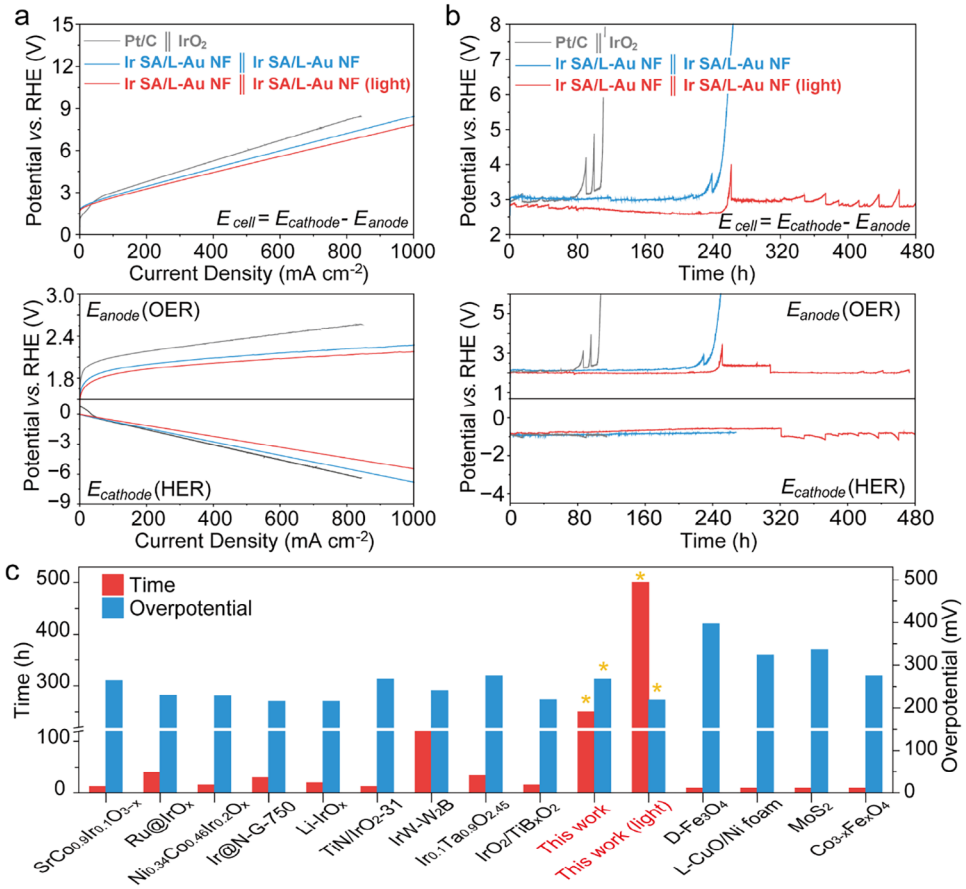


Figure 5. Overall water splitting performance. a) Polarization *I–V* profiles of various catalysts measured in 0.5 M H_2SO_4. b) Chronopotentiometric stability profiles measured at 100 mA cm^{-2} for 480 h. c) Comparison of the overall water electrolysis stability of various catalysts reported in the literature.

dominate the catalytic enhancement, as opposed to mere thermal effects.

Under illumination, the Ir SA/L-Au NF electrode not only excels in OER but also demonstrates exceptional HER performance, comparable to platinum on carbon (Pt/C), the leading HER catalyst (Figures S29–S33, Supporting Information). Electrochemical measurements revealed that the Ir SA/L-Au NF electrode achieved an overpotential and Tafel slope close to those of Pt/C. Additionally, the Ir SA/L-Au NF delivered competitive mass activities and exhibited a higher ECSA than its counterparts, leading to improved exposure to reactants and enhanced reaction kinetics (Figure S32, Supporting Information).

To support this, ECSA-normalized HER activity was also evaluated and is shown in Figure S34 (Supporting Information). The overpotential at 10 mA cm^{-2} after ECSA normalization shows that Ir SA/L-Au NF under light maintains its superior performance compared to the other samples, confirming its enhanced intrinsic catalytic activity beyond geometric or mass normalization. Furthermore, although a ≈50% higher ECSA is observed for Ir SA/L-Au NF under light, the improvement in HER overpotential cannot be attributed solely to increased surface area. The ECSA-normalized overpotential data (Figure S34b, Supporting Information) confirm that the light-enhanced catalyst still outperforms others intrinsically. Therefore, the performance gain arises from spin polarization-driven modifications in surface chemistry, consistent with the Sabatier principle and CISS effect.

Further investigation confirmed that plasmon-induced hot carriers were primarily responsible for the enhanced HER performance, far surpassing the effects of pure thermal activation. These results underscore the dual utility of Ir SA/L-Au NF under illumination for both OER and HER, establishing it as a highly effective and durable catalyst for water-splitting applications.

2.4. Overall Water Splitting by Ir SA/L-Au NF/Ti || Ir SA/L-Au NF/Ti

In a comprehensive evaluation of the newly developed Ir SA/L-Au NF electrode, we conducted an overall water splitting test in an acidic medium of 0.5 M H_2SO_4 using a three-electrode configuration with an Ag/AgCl reference electrode. This setup effectively separated the overall cell reaction into its constituent HER and OER parts. As illustrated in Figure S35 (Supporting Information), the active generation of hydrogen and oxygen gases at the cathode and anode, respectively, was observed during the electrochemical water electrolysis.

Figure 5a details the HER and OER polarization curves denoted as $E_{cathode}$ and E_{anode}. These curves, recorded during the

© 2025 The Author(s). Advanced Materials published by Wiley-VCH GmbH

15214095, 2025, 39, Downloaded from https://advanced.onlinelibrary.wiley.com/doi/10.1002/adma.202507658 by Ewha Womans University Library, Wiley Online Library on [13/01/2026]. See the Terms and Conditions (https://onlinelibrary.wiley.com/terms-and-conditions) on Wiley Online Library for rules of use; OA articles are governed by the applicable Creative Commons License

water electrolysis, were critical in determining the cell potentials ($E_{cell} = E_{anode} - E_{cathode}$). We compared the cell potentials of the conventional Pt/C || IrO_2 system and our novel Ir SA/L-Au NF/Ti || Ir SA/L-Au NF/Ti arrangement under both light and no light conditions. This comparison was pivotal in establishing the efficiency of the Ir SA/L-Au NF electrode in water splitting. Furthermore, the electrochemical stability and durability of the Ir SA/L-Au NF/Ti electrode were assessed through chronopotentiometric profiles at a current density of 100 mA cm^{-2} (Figure 5b). While the Pt/C || IrO_2 setup showed gradual degradation and eventual failure after 100 h, the Ir SA/L-Au NF/Ti || Ir SA/L-Au NF/Ti system maintained stable operation over 250 h with minimal performance fluctuation. Remarkably, under light irradiation, this stability extended beyond 480 h, underscoring the electrode's exceptional durability in both HER and OER, even at high current densities.

Figures S36 and S37 (Supporting Information), display SEM images of the Ir SA/L-Au NF electrode after stability testing under both dark and illuminated conditions. The electrode exposed to light showed fewer signs of clogging or physical damage compared to the one tested in the dark, highlighting the protective role of light irradiation in maintaining structural integrity during prolonged operational testing. XPS analysis revealed that the chemical state of the electrode remained largely unchanged after 480 h. Figure S38a (Supporting Information) shows that the cathode's Ir 4f spectrum remained stable, while Figure S38b (Supporting Information), indicates a slight shift in the anode's Ir 4f spectrum toward lower binding energy under light. Under light conditions, the Ir SA/L-Au NF electrode displayed a distinct XPS spectrum with a clear split into two doublets, even after 480 h of testing, unlike in the dark. To further evaluate structural stability, XRD patterns were obtained before and after stability testing (Figure S39, Supporting Information). For the cathode, both dark and light conditions maintained distinct Au diffraction peaks, indicating good structural retention of the Au nanoflowers. However, in the anode samples, a significant difference was observed: while the Au peaks remained under illumination, their intensity decreased, and notably, the Au peaks nearly disappeared in the dark. This suggests that light irradiation not only preserves the Au nanostructure on the cathode but also mitigates the degradation of Au components at the anode during extended electrochemical operation. This underscores the exceptional stability of the Ir SA/L-Au NF electrode as a light-driven electrocatalyst. In Figure 5c and Tables S2 and S3 (Supporting Information), our catalyst's stability surpasses that of other prominent water splitting catalysts, even under high current density conditions.

2.5. Theoretical Insights and *Operando* X-Ray Spectroscopy

To further understand the OER mechanism influenced by the CISS effect, a theoretical study based on density functional theory (DFT) calculations was conducted (Figure S40, Supporting Information). The energy diagrams reveal that the overpotential for the OER reaction decreases from 0.66 to 0.46 V when the Au surface is spin-polarized (Figure S40a,b, Supporting Information). This reduction aligns with experimental observations and improves the OER reaction. Magnetic density maps further illustrate that this reduction is linked to the CISS effect (Figure S40c,d, Supporting Information). On a non-spin-polarized Au surface, neither the Ir atom nor the reaction intermediates show significant magnetic moments. However, on the spin-polarized Au surface, the Ir atom exhibits a pronounced magnetic moment, and the oxygen atoms in the reaction intermediates demonstrate clear spin polarization. This spin alignment provides strong evidence of the CISS effect's pivotal role in enhancing the OER process.

Additionally, DFT calculations were used to investigate the HER mechanism and its enhanced performance on the Ir SA/L-Au NF electrode (Figure S41, Supporting Information). The overpotential on the spin-polarized Au surface was found to be 0.12 eV, substantially lower than the 0.86 eV observed on the non-spin-polarized Au surface (Figure S41a, Supporting Information). While the product of HER, H_2, is a spin-singlet, the CISS effect modulates HER activity by influencing the adsorption characteristics of the atomic hydrogen (H) intermediate, rather than affecting the spin state of the final H_2 molecule. The observed decrease in overpotential is therefore closely linked to modification in the bonding characteristics around the Ir single atom. Electron localization function analysis shows that spin polarization weakens the covalency of the H—Ir—Au bond, reducing the hydrogen atom's adsorption energy (Figure S41b,c, Supporting Information). This is further supported by the density of states (DOS) analysis, which reveals that hybridization between H, Ir, and Au below the Fermi energy is significantly reduced on the spin-polarized surface (Figure S41d–g, Supporting Information). These findings indicate that spin alignment primarily alters the surface electronic structure and intermediate adsorption energies, enhancing reaction kinetics without influencing the spin state of the H_2 molecule itself.

To clarify the origins of the exceptional OER catalytic activity and enhanced structural stability of Ir SA/L-Au NF under light irradiation, we examined the dynamic changes in the oxidation state and local structural environment using *operando* XAS analysis. **Figure 6**a,b present the normalized operando Ir L_3-edge XANES spectra and the corresponding FT-EXAFS spectra. The white line position as a function of the d-band hole and the variations in Ir—O and Ir—Au bond lengths are analyzed in Figure 6c,d. Under open-circuit voltage (OCV), the white line position of Ir-SA/L-Au NF shifted to higher energy, with an increase in d-band holes due to the chemisorption of OH^- and H_2O molecules.[35,36] During electrochemical OER at 1.45 V versus RHE, the d-band holes increased to 4.48, indicating the formation of Ir intermediates (e.g., OOH*) and stronger OH^- and H_2O chemisorption.[37] Under light irradiation, the d-band holes increased further, with a shift in the white line position driven by hot carriers generated from LSPRs on the chiral Au substrates.[38,39]

The Ir—O bond in Ir-SA/L-Au NF contracted slightly at 1.45 V versus RHE compared to OCV, consistent with a typical decrease in transition metal-oxygen bond distance as the metal ion's redox state increases due to a reduction in its ionic radius (Figure 6d).[40,41] However, under light at the same potential, the Ir—Au bond length decreased significantly, while the Ir—O bond remained unchanged. This contraction of Ir—Au bonds stabilizes the isolated Ir single atoms, preventing agglomeration and degradation, thereby preserving active sites.[42] This shrinkage of Ir—Au bonds induced by LSPRs directly correlates with improved OER stability under plasmonic excitation (Figure 5b).

© 2025 The Author(s). Advanced Materials published by Wiley-VCH GmbH

15214095, 2025, 39, Downloaded from https://advanced.onlinelibrary.wiley.com/doi/10.1002/adma.202507658 by Ewha Womans University Library, Wiley Online Library on [13/01/2026]. See the Terms and Conditions (https://onlinelibrary.wiley.com/terms-and-conditions) on Wiley Online Library for rules of use; OA articles are governed by the applicable Creative Commons License

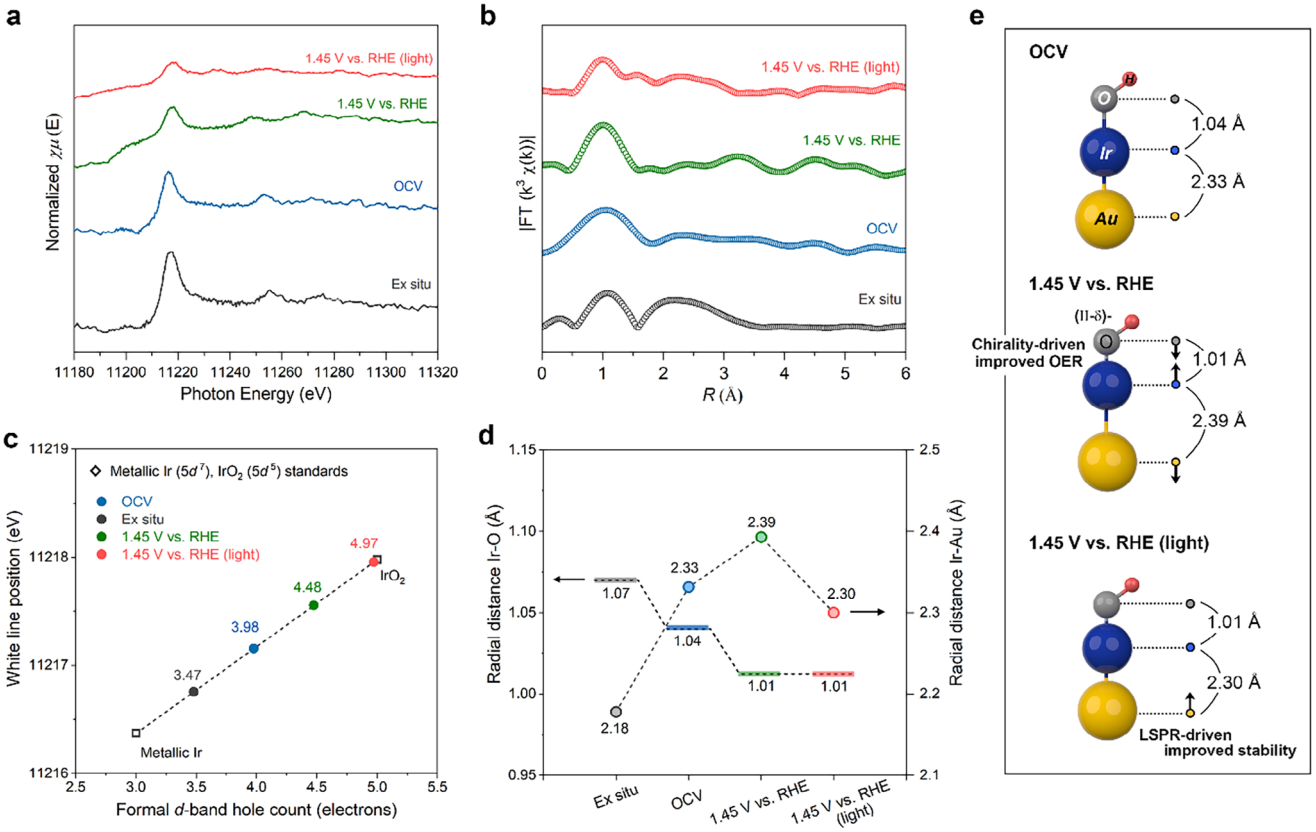


Figure 6. *Operando* XAFS spectra of Ir L_3-edge under plasmon-assisted electrochemical conditions. a) *Operando* Ir L-edge XANES of Ir SA/L-Au NF under different applied potentials with/without plasmonic condition, and ex situ XANES spectra of the reference standards of Ir SA/L-Au NF b) Corresponding FT-EXAFS spectra from (a). c) White line position of each condition as a function of the formal d-band hole count. d) The fitted variation of the Ir—O bond and Ir—Au bond at different conditions. e) Schematic illustration of the bonding relaxation and shrinkage during the OER process under light irradiation.

Consequently, the synergistic effects of spin alignment from the chiral substrate and strengthened Ir—Au bonding via LSPRs are essential for the outstanding OER activity and stability of Ir-SA/L-Au NF. Spin alignment enhances catalytic efficiency, while the contraction of Ir—Au bonds under light prevents the degradation of Ir single atoms, ensuring durability and high performance (Figure 6e).

3. Conclusion

Our approach showcases a substantial enhancement in catalytic efficiency for both OER and HER by integrating a single-atom catalyst reactor with chiral plasmonic effects. We introduce a plasmonic antenna-reactor hybrid catalyst, where spin-polarized hot electrons generated from the Au antenna are injected into the active sites of the Ir SAC reactor. The precise electrodeposition process optimizes Ir single-atom loading, resulting in a highly efficient catalyst architecture. The Ir SA/L-Au NF/Ti || Ir SA/L-Au NF/Ti electrode system delivers exceptional stability, sustaining continuous water splitting for over 480 h at a high current density of 100 mA cm^{-2} in acidic conditions, far surpassing conventional Pt/C || IrO_2 systems, achieving a 3.5 fold increase in reaction kinetics (at 1.57 V vs RHE) compared to commercial IrO_2 catalysts and enhancing durability by over 4.8 times relative to conventional Pt/C || IrO_2 systems. Supported by DFT calculations and *operando* XAS analysis, our findings demonstrate the critical role of photogenerated hot electrons and the CISS effect in boosting OER and HER performance. The plasmon-driven spin alignment induces polarization in the Ir atoms, stabilizing their structure and maintaining the electrode's integrity throughout extended operation. This innovative approach highlights the potential for light-driven electrocatalysis in developing efficient, stable, and cost-effective solutions for sustainable energy conversion.

4. Experimental Section

Preparation of L-Au NF/Ti: Achiral and chiral gold electrodepositions were carried out by a typical three-electrode system with the Ti felt substrate as the working electrode, a graphite rod utilized as a counter electrode, and a Ag/AgCl electrode serving as a reference electrode in a precursor solution consisting of 2 mM $HAuCl_4 \cdot 3H_2O$ in 0.1 M KCl with 0.05 mM of DL/D/L-Cysteine at the room temperature. The electrodeposition process was carried out through constant potential electrolysis at 0 V versus Ag/AgCl for 300 s using a potentiostat (Autolab electrochemical analyzer). As-prepared L-Au NF/Ti electrode was rinsed with deionized water and then dried at room temperature.

Preparation of Ir SA/L-Au NF/Ti: The Ir single atom deposition on L-Au NF/Ti was carried out by a typical three-electrode system, and an

© 2025 The Author(s). Advanced Materials published by Wiley-VCH GmbH

15214095, 2025, 39, Downloaded from https://advanced.onlinelibrary.wiley.com/doi/10.1002/adma.202507658 by Ewha Womans University Library, Wiley Online Library on [13/01/2026]. See the Terms and Conditions (https://onlinelibrary.wiley.com/terms-and-conditions) on Wiley Online Library for rules of use; OA articles are governed by the applicable Creative Commons License

Ag/AgCl electrode was utilized as the reference electrode. The precursor solution consisted of 100 uM $IrCl_4$ and 1 M KOH at room temperature. The electrochemical deposition was carried out from 0.10 to −0.40 V versus RHE for twenty periods with a sweeping rate of 5 mV s^{-1}. Finally, the electrode was washed with deionized water and dried at room temperature.

Material Characterizations: The morphologies of the as-prepared sample were examined by high-resolution SEM (HR-SEM) and TEM on JSM-7610F and JEM-2100F systems. HAADF-STEM and EDS results were obtained on a FEI (TitanTM 80–300) instrument. Powder XRD patterns were collected under Ni filtered Cu-Kα radiation ($\lambda = 1.5418$ Å) in the 20°–80° 2θ region without air exposure using a Rigaku Dmax 2000 diffractometer. XPS was performed on a Thermo Scientific K-Alpha XPS, using a dual-beam source and ultra-low energy electron beam. X-ray absorption spectroscopy (XAS) data were obtained by using the TPS 44A and TLS 17C1 beamline from the National Synchrotron Radiation Research Center (NSRRC) in Hsinchu, Taiwan.

The CD spectra were recorded on a JASCO J-1500 CD spectrometer. In addition, mc-AFM (SPA400, Seiko Instruments) was performed in an area of 2 um x 2 um using a Co-Cr-coated cantilever to investigate the electrical properties of the devices. Prior to the measurement, tips were premagnetized by a strong permanent magnet for >60 min. For all samples, *I–V* curves were measured by sweeping the voltage from −1.0 to +1.0 V with a frequency of 0.5 Hz. In each of the mc-AFM measurements, the average value was obtained from 30 times of *I–V* sweeps with different positions and samples.

Electrochemical Measurement: All electrochemical measurements were carried out in a typical three-electrode system with an electrochemical workstation (SP150) at room temperature, using a graphite rod as the counter electrode and Ag/AgCl as the reference electrode. Then, OER and HER profiles were investigated in 0.5 M H_2SO_4 aqueous solution at a scan rate of 10 mV s^{-1} with as-prepared electrodes, where the area is 1 cm^2. All electrochemical tests were carried out using a 1.5 AG 300 W Xe lamp as the light source.

The formation of H_2O_2 was measured by spectrophotometric titration of the used electrolyte, with the $TiOSO_4$-containing aqueous solution (1.9–2.1%, Sigma–Aldrich) using a UV–vis spectrometer (SHIMADZU, UV-3600i Plus).

$$Ti^{4+} + H_2O_2 + 2H_2O \rightarrow H_2TiO_4 + 4H^+ \quad (2)$$

Overall Water Splitting Test: The overall water electrolysis tests were conducted in the three-electrode configuration using an Ag/AgCl reference electrode. The cathode and anode were prepared onto a Ti felt with an area of 1 cm^2. The measurements were performed in 0.5 M H_2SO_4 aqueous solution.

Operando XAFS Measurements: To fabricate, Iridium L_3-edge X-ray Absorption Fine Structure (XAFS) experiments were performed at the Pohang Light Source (PLS-II), Korea, with the storage ring set at 10 GeV and a stable current of 3 kA. XAFS data were acquired in fluorescence mode using ion chambers, and the data were processed for background subtraction and normalization using Athena software. *Operando* XAFS measurements were conducted using an Ir SA/L-Au NF electrode in a specially designed cell with 0.5 M H_2SO_4 as the electrolyte. The Ir SA/L-Au NF electrodeposited electrode acted as the working electrode, a graphite rod served as the counter electrode, and Ag/AgCl was used as the reference electrode in the electrochemical setup. XAFS data collection was completed within a single beam time period, and the white-line position showed consistency across all scans, indicating reliable measurements.

Calculation Details: First-principles density functional theory (DFT) calculations were performed using the projector-augmented-wave method[43] and the Perdew–Burke–Ernzerhof functional[44] as implemented in the Vienna Ab initio Simulation Program code.[45] The 5d and 6s electrons of Au, the 5d and 6s electrons of Ir, the 2s and 2p electrons of O, and the 1s electron of H were used as valence electrons. A plane-wave basis cut-off energy was set to 450 eV. A slab model for the (111) surface of Au was constructed as (2 × 2) stoichiometric supercells with a vacuum of 30 Å along the c-axis. The 6 × 6 × 6 and 2 × 2 × 1 k-point meshes were used for the unit cell and slab, respectively. Structural relaxation was performed until the Hellmann–Feynman forces were less than 5×10^{-2} eV $Å^{-1}$. To simulate the non-spin-polarized state of the Ir SA/DL-Au NF slab, full electronic relaxation was performed by setting the initial magnetic moment of all Au atoms to 0 μ_B. For the spin-polarized configuration of the Ir SA/L-Au NF slab corresponding to the excited state induced by the CISS effect, the initial magnetic moment of each Au atom was set to 1 μ_B. In addition, the difference between the total number of spin-up and spin-down electrons in the entire system was constrained to 96, which corresponded to the number of Au atoms in the slab. This constraint ensured that the system retained its spin-polarized character and did not relax back to the non-magnetic ground state. The spin distribution across the system was obtained through self-consistent electronic relaxation, allowing each atom to achieve its thermodynamically stable spin configuration under the global spin.[46,47] For the relaxation of the slab, the topmost layer was relaxed while keeping the last layer frozen. The crystal structures, magnetic density maps, and electron localization functions were visualized using the VESTA code.[48]

Supporting Information

Supporting Information is available from the Wiley Online Library or from the author.

Acknowledgements

This work was supported by the Basic Science Research Program (Priority Research Institute) through the National Research Foundation (NRF) of Korea funded by the Ministry of Education (2021R1A6A1A10039823) and by the Korea Basic Science Institute (National Research Facilities and Equipment Center) grant funded by the Ministry of Education (2020R1A6C101B194). J.K. acknowledges the financial support from the NRF grant funded by the Korea government (MSIT) (No. RS-2023-00212105). R.S.L. thanks the National Science and Technology Council of Taiwan (NSTC 113-2113-M-002-005). This work was sponsored by Syensqo.

Conflict of Interest

The authors declare no conflict of interest.

Data Availability Statement

The data that support the findings of this study are available from the corresponding author upon reasonable request.

Keywords

CISS effect, plasmonic effect, single atom catalysis, stability, water splitting

Received: April 22, 2025
Published online: June 26, 2025

[1] M. S. Dresselhaus, I. L. Thomas, *Nature* **2001**, *414*, 332.
[2] S. Chu, A. Majumdar, *Nature* **2012**, *488*, 294.
[3] Q. Wang, C.-Q. Xu, W. Liu, S.-F. Hung, H. B. Yang, J. Gao, W. Cai, H. M. Chen, J. Li, B. Liu, *Nat. Commun.* **2020**, *11*, 4246.
[4] F.-Y. Chen, Z.-Y. Wu, Z. Adler, H. Wang, *Joule* **2021**, *5*, 1704.

© 2025 The Author(s). Advanced Materials published by Wiley-VCH GmbH

15214095, 2025, 39, Downloaded from https://advanced.onlinelibrary.wiley.com/doi/10.1002/adma.202507658 by Ewha Womans University Library, Wiley Online Library on [13/01/2026]. See the Terms and Conditions (https://onlinelibrary.wiley.com/terms-and-conditions) on Wiley Online Library for rules of use; OA articles are governed by the applicable Creative Commons License

[5] T. Tang, W.-J. Jiang, S. Niu, N. Liu, H. Luo, Y.-Y. Chen, S.-F. Jin, F. Gao, L.-J. Wan, J.-S. Hu, *J. Am. Chem. Soc.* **2017**, *139*, 8320.
[6] F. Yu, H. Zhou, Y. Huang, J. Sun, F. Qin, J. Bao, W. A. Goddard III, S. Chen, Z. Ren, *Nat. Commun.* **2018**, *9*, 2551.
[7] W. Xiang, N. Yang, X. Li, J. Linnemann, U. Hagemann, O. Ruediger, M. Heidelmann, T. Falk, M. Aramini, S. DeBeer, M. Muhler, K. Tschulik, T. Li, *Nat. Commun.* **2022**, *13*, 179.
[8] F. Zhao, B. Wen, W. Niu, Z. Chen, C. Yan, A. Selloni, C. G. Tully, X. Yang, B. E. Koel, *J. Am. Chem. Soc.* **2021**, *143*, 15616.
[9] G. Zhao, P. Li, N. Cheng, S. X. Dou, W. Sun, *Adv. Mater.* **2020**, *32*, 2000872.
[10] H. You, D. Wu, D. Si, M. Cao, F. Sun, H. Zhang, H. M. Wang, T.-F. Liu, R. Cao, *J. Am. Chem. Soc.* **2022**, *144*, 9254.
[11] Z. Lei, W. Cai, Y. Rao, K. Wang, Y. Jiang, Y. Liu, X. Jin, J. Li, Z. Lv, S. Jiao, W. Zhang, P. Yan, S. Zhang, R. Cao, *Nat. Commun.* **2022**, *13*, 24.
[12] A. Vadakkayil, C. Clever, K. N. Kunzler, S. Tan, B. P. Bloom, D. H. Waldeck, *Nat. Commun.* **2023**, *14*, 1067.
[13] F. A. Garcés-Pineda, M. Blasco-Ahicart, D. Nieto-Castro, N. López, J. R. Galán-Mascarós, *Nat. Energy* **2019**, *4*, 519.
[14] R. Naaman, D. H. Waldeck, *J. Phys. Chem. Lett.* **2012**, *3*, 2178.
[15] R. Naaman, Y. Paltiel, D. H. Waldeck, *J. Phys. Chem. Lett.* **2020**, *11*, 3660.
[16] B. Göhler, V. Hamelbeck, T. Z. Markus, M. Kettner, G. F. Hanne, Z. Vager, R. Naaman, H. Zacharias, *Science* **2011**, *331*, 894.
[17] R. Naaman, D. H. Waldeck, *Annu. Rev. Phys. Chem.* **2015**, *66*, 263.
[18] R. Naaman, Y. Paltiel, D. H. Waldeck, *Acc. Chem. Res.* **2020**, *53*, 2659.
[19] M. P. S. Rodrigues, A. H. B. Dourado, L. O. Cutolo, L. S. Parreira, T. V. Alves, T. J. A. Slater, S. J. Haigh, P. H. C. Camargo, S. I. C. Torresi, *ACS Catal.* **2021**, *11*, 13543.
[20] U. Aslam, V. G. Rao, S. Chavez, S. Linic, *Nat. Catal.* **2018**, *1*, 656.
[21] G. Baffou, R. Quidant, *Chem. Soc. Rev.* **2014**, *43*, 3898.
[22] S. J. Freakley, J. Ruiz-Esquius, D. J. Morgan, *Surf. Interface Anal.* **2017**, *49*, 794.
[23] H. Kim, J. Kim, J. Kim, G. H. Han, W. Guo, S. Hong, H. S. Park, H. W. Jang, S. Y. Kim, S. H. Ahn, *Appl. Catal. B* **2021**, *283*, 119596.
[24] E. Bailón-García, F. Carrasco-Marín, A. F. Pérez-Cadenas, F. J. Maldonado-Hódar, *Appl. Catal. A Gen.* **2016**, *512*, 63.
[25] H. Wang, Z. Chen, D. Wu, M. Cao, F. Sun, H. Zhang, H. You, W. Zhuang, R. Cao, *J. Am. Chem. Soc.* **2021**, *143*, 4639.
[26] F. Liao, K. Yin, Y. Ji, W. Zhu, Z. Fan, Y. Li, J. Zhong, M. Shao, Z. Kang, Q. Shao, *Nat. Commun.* **2023**, *14*, 1248.
[27] Y. Zhu, J. Wang, T. Koketsu, M. Kroschel, J.-M. Chen, S.-Y. Hsu, G. Henkelman, Z. Hu, P. Strasser, J. Ma, *Nat. Commun.* **2022**, *13*, 7754.
[28] K. B. Ghosh, W. Zhang, F. Tassinari, Y. Mastai, O. Lidor-Shalev, R. Naaman, P. Möllers, D. Nürenberg, H. Zacharias, J. Wei, E. Wierzbinski, D. H. Waldeck, *J. Phys. Chem. C* **2019**, *123*, 3024.
[29] H. Lee, S. Ma, S. Oh, J. Tan, C. U. Lee, J. Son, Y. S. Park, J. Yun, G. Jang, J. Moon, *Small* **2023**, *19*, 2304166.
[30] H. Im, S. Ma, H. Lee, J. Park, Y. S. Park, J. Yun, J. Lee, S. Moon, J. Moon, *Energy Environ. Sci.* **2023**, *16*, 1187.
[31] J. Wei, H. Tang, L. Sheng, R. Wang, M. Fan, J. Wan, Y. Wu, Z. Zhang, S. Zhou, J. Zeng, *Nat. Commun.* **2024**, *15*, 559.
[32] W. Zhang, K. Banerjee-Ghosh, F. Tassinari, R. Naaman, *ACS Energy Lett.* **2018**, *3*, 2308.
[33] L. Zhou, D. F. Swearer, C. Zhang, H. Robatjazi, H. Zhao, L. Henderson, L. Dong, P. Christopher, E. A. Carter, P. Nordlander, N. J. Halas, *Science* **2018**, *362*, 69.
[34] L. Zhou, J. M. P. Martirez, J. Finzel, C. Zhang, D. F. Swearer, S. Tian, H. Robatjazi, M. Lou, L. Dong, L. Henderson, P. Christopher, E. A. Carter, P. Nordlander, N. J. Halas, *Nat. Energy* **2020**, *5*, 61.
[35] Y. Yao, S. Hu, W. Chen, Z.-Q. Huang, W. Wei, T. Yao, R. Liu, K. Zang, X. Wang, G. Wu, W. Yuan, T. Yuan, B. Zhu, W. Liu, Z. Li, D. He, Z. Xue, Y. Wang, X. Zheng, J. Dong, C.-R. Chang, Y. Chen, X. Hong, J. Luo, S. Wei, W.-X. Li, P. Strasser, Y. Wu, Y. Li, *Nat. Catal.* **2019**, *2*, 304.
[36] H. N. Nong, T. Reier, H.-S. Oh, M. Gliech, P. Paciok, T. H. T. Vu, D. Teschner, M. Heggen, V. Petkov, R. Schlögl, T. Jones, P. Strasser, *Nat. Catal.* **2018**, *1*, 841.
[37] X. Tian, X. Zhao, Y.-Q. Su, L. Wang, H. Wang, D. Dang, B. Chi, H. Liu, E. J. M. Hensen, X. W. Lou, B. Y. Xia, *Science* **2019**, *366*, 850.
[38] Z. Wu, X. Liu, H. Li, Z. Sun, M. Cao, Z. Li, C. Fang, J. Zhou, C. Cao, J. Dong, S. Zhao, Z. Chen, *Nat. Commun.* **2023**, *14*, 2574.
[39] L. Huang, J. Zou, J.-Y. Ye, Z.-Y. Zhou, Z. Lin, X. Kang, P. K. Jain, S. Chen, *Angew. Chem., Int. Ed.* **2019**, *58*, 8794.
[40] J.-H. Choy, D.-K. Kim, S.-H. Hwang, G. Demazeau, D.-Y. Jung, *J. Am. Chem. Soc.* **1995**, *117*, 8557.
[41] M. Görlin, P. Chernev, J. F. Araújo, T. Reier, S. Dresp, B. Paul, R. Krähnert, H. Dau, P. Strasser, *J. Am. Chem. Soc.* **2016**, *138*, 5603.
[42] P. Li, M. Wang, X. Duan, L. Zheng, X. Cheng, Y. Zhang, Y. Kuang, Y. Li, Q. Ma, Z. Feng, W. Liu, X. Sun, *Nat. Commun.* **2019**, *10*, 1711.
[43] P. E. Blöchl, *Phys. Rev. B* **1994**, *50*, 17953.
[44] J. P. Perdew, K. Burke, M. Ernzerhof, *Phys. Rev. Lett.* **1996**, *77*, 3865.
[45] G. Kresse, J. Furthmüller, *Phys. Rev. B* **1996**, *54*, 11169.
[46] T. Wu, Y. Sun, X. Ren, J. Wang, J. Song, Y. Pan, Y. Mu, J. Zhang, Q. Cheng, G. Xian, S. Xi, C. Shen, H.-J. Gao, A. C. Fisher, M. P. Sherburne, Y. Du, J. W. Ager, J. Gracia, H. Yang, L. Zeng, Z. J. Xu, *Adv. Mater.* **2023**, *35*, 2207041.
[47] A. De, C. M. Perez, A. Liang, K. Wang, L. Dou, O. Prezhdo, L. Huang, *J. Am. Chem. Soc.* **2024**, *146*, 4260.
[48] K. Momma, F. Izumi, *J. Appl. Cryst.* **2011**, *4*, 1272.

© 2025 The Author(s). Advanced Materials published by Wiley-VCH GmbH

15214095, 2025, 39, Downloaded from https://advanced.onlinelibrary.wiley.com/doi/10.1002/adma.202507658 by Ewha Womans University Library, Wiley Online Library on [13/01/2026]. See the Terms and Conditions (https://onlinelibrary.wiley.com/terms-and-conditions) on Wiley Online Library for rules of use; OA articles are governed by the applicable Creative Commons License